RSC Advances

PAPER

View Article Online
View Journal | View Issue

Check for updates

Cite this: *RSC Adv.*, 2026, **16**, 16181

Water-hyacinth-leaf-like 2D bismuth oxychloride photocatalyst for the degradation of methylene blue and crystal violet dyes

Rajvardhan K. Chougale,[ae] Prashant D. Sanadi,[a] Sharadchandra S. Patil,[b] Umesh S. Siddharth,[c] Pravin P. Pawar,[d] Babasaheb D. Bhosale*[e] and Ganesh S. Kamble *[a]

Received 10th February 2026
Accepted 9th March 2026

DOI: 10.1039/d6ra01208f

rsc.li/rsc-advances

In this research, we synthesized a water-hyacinth (*Eichhornia crassipes*)-leaf-like 2D bismuth oxychloride (Bi_3ClO_4) photocatalyst using a simple co-precipitation method. The as-synthesized Bi_3ClO_4 is characterized by XRD, Raman spectroscopy, UV-vis spectroscopy, SEM, EDAX and BET analysis. The XRD results showed that the material has a monoclinic crystal structure. Raman spectroscopy confirmed the existence of the vibrational bands of bismuth oxychloride. The BET surface area measurement indicated that the material has a porous structure with a surface area of 13.68 $m^2\ g^{-1}$. The SEM analysis revealed that the material has a well-defined nanostructured sheet-like morphology. The EDAX study showed that the synthesized material has a well-defined stoichiometry. The as-synthesized bismuth oxychloride photocatalyst exhibited enhanced photocatalytic activity under visible-light irradiation. Complete degradation of crystal violet (100%) was achieved within 75 min, while methylene blue showed 96% degradation within 105 min. These findings highlight the strong potential of bismuth oxychloride as an efficient photocatalyst for wastewater remediation.

1 Introduction

Rapid industrialization and urban expansion have led to the extensive discharge of synthetic dyes into natural water bodies, posing severe environmental and health challenges. Industries such as textile, leather, paper, plastic, and pharmaceuticals are significant contributors to dye-laden wastewater, releasing substantial quantities of colored effluents annually.[1–4] These dyes are often chemically stable, non-biodegradable, and resistant to conventional wastewater treatment processes, enabling them to persist in aquatic ecosystems for long durations.[5–8] The presence of dyes in water bodies not only imparts intense coloration, which reduces light penetration and disrupts photosynthetic activities, but also introduces toxic, mutagenic, and carcinogenic compounds into the environment. Many azo and anthraquinone dyes decompose into aromatic amines, which are harmful to aquatic organisms and may bioaccumulate through the food chain, posing risks to human health.[9–12] Therefore, the development of efficient and sustainable dye removal technologies has become a critical area of environmental research.

Among various remediation strategies such as adsorption, coagulation, membrane filtration, and biological treatment, advanced oxidation processes (AOPs) have gained significant attention due to their ability to completely mineralize organic pollutants into harmless end-products like CO_2 and H_2O.[13–16] Photocatalysis, a key AOP, utilizes semiconductor materials to generate highly reactive oxygen species (ROS) under light irradiation, enabling the effective degradation of complex dye molecules.[17–19] Nanomaterials have gained significant attention as promising photocatalysts owing to their high surface-to-volume ratios, tunable electronic structures, and enhanced charge carrier dynamics.[20] In particular, bismuth-based oxyhalides and oxychlorides have attracted increasing interest due to their layered crystal structures, suitable band gaps, and strong internal electric fields that facilitate the efficient separation of photogenerated electron–hole pairs.[21–25]

Recently, bismuth oxychloride derivatives, such as Bi_3ClO_4, have been explored as advanced photocatalysts for dye degradation applications. Bi_3ClO_4 exhibits a unique crystal structure that combines favourable light absorption and improved redox capability, enabling the effective generation of reactive oxygen species under visible light irradiation.[26–28] Compared with conventional photocatalysts such as TiO_2, BiOCl, Bi_2O_3–TiO_2, Bi_2O_3/g-C_3N_4, and $Zn_3(VO_4)_2$, $BiVO_4$-derived heterostructures and nanocomposite photocatalysts have exhibited efficient

[a]*Department of Engineering Chemistry, Kolhapur Institute of Technology's College of Engineering (Empowered Autonomous), Kolhapur (Affiliated to Shivaji University Kolhapur), 416234, India. E-mail: ganeshchemistry2010@gmail.com; kamble.ganesh@kitcoek.in*

[b]*Department of Physics, Shivaji University Kolhapur, 416004, India*

[c]*Sangrul High School and Jr. College, Sangrul, Dist., Kolhapur, India*

[d]*Department of Medical Physics, Center for Interdisciplinary Research, D. Y. Patil Education Society Kolhapur (Deemed to be University), 416006, India*

[e]*Department of Chemistry, Rajaram College Kolhapur (Affiliated to Shivaji University Kolhapur), 416004, India. E-mail: babasahebbhosale23@gmail.com*

Open Access Article. Published on 23 March 2026. Downloaded on 4/30/2026 8:36:08 PM. This article is licensed under a Creative Commons Attribution-NonCommercial 3.0 Unported Licence.

Open Access Article. Published on 23 March 2026. Downloaded on 4/30/2026 8:36:08 PM. This article is licensed under a Creative Commons Attribution-NonCommercial 3.0 Unported Licence.

Table 1 Comparison of the photocatalytic performance of the as-synthesized Bi_3ClO_4 nanomaterial with reported photocatalysts

S. no.	Catalyst	Organic pollutant	Light source	Degradation time (min)	Degradation efficiency (%)	Rate constant (min^{-1})	Ref.
1	BiOCl	MB	UV-vis	90	100	0.038	29
2	Bi_2O_3–TiO_2	MB	UV-vis	90	100	0.038	30
3	Bi_2O_3/g-C_3N_4	MB	Visible	100	98	—	31
4	$Zn_3(VO_4)_2$	MB	Visible	120	87	0.010–0.017	32
5	ZnO	MB	Visible	180–300	97–100	—	33
6	$BiIO_4$/$BiVO_4$	RhB	Visible	60	98	0.05	34
7	$BiVO_4$/TiS_2	RhB	Visible	70	95	—	35
8	ZnO	CV	UV	80	90		36
9	ZnO and C/ZnO	CV	UV	60	92	—	37
10	ZnO	CV	UV	30	98	—	38
11	$BiVO_4$–$NiFe_2O_4$	CV	UV	60	95	—	39
12	Ag_2S/NiO–ZnO	RhB	Visible light	120	95	0.0302	40
13	In_2O_3/CeO_2	Congo red (CR), methylene blue (MB)	Visible light	91 (CR) and 130 (MB)	95 (CR) and 94 (MB)	—	41
14	Ag_2O/ZnO–TiO_2	RhB	Visible light	100	95	0.0129	42
15	Ag_2CO_3–$BiVO_4$	Tetracycline	Visible light	80	94	0.0278	43
16	$LaFe_2O_3$/Sb_2O_3	Malachite green (MG)	Visible light	88	98 (RhB)	0.003399	44
17	10 mg of Bi_3ClO_4	Methylene blue	Visible	105	96		This work
		Crystal violet	Visible	75	100		This work

degradation of model organic pollutants including methylene blue (MB), rhodamine B (RhB), and crystal violet (CV) under UV or visible irradiation (Table 1).[29–44] Despite achieving high degradation efficiencies (≈90–100%), many reported catalysts depend on UV irradiation or longer reaction durations and are associated with the formation of potentially toxic by-products. In this context, the development of simple, visible-light-responsive bismuth-based photocatalysts with rapid degradation kinetics remains an important research objective. Motivated by these considerations, the present work explores Bi_3ClO_4 as an efficient photocatalyst for the degradation of MB and CV under visible light. The obtained results demonstrate competitive performance compared with previously reported systems, indicating that Bi_3ClO_4 shows superior and promising visible light responsiveness, making it suitable for solar-driven wastewater treatment processes.[45] Furthermore, the photocatalytic performance of Bi_3ClO_4 can be significantly enhanced through nanostructuring, defect engineering, and heterojunction formation, which improve light harvesting and suppress charge recombination.[46,47] These attributes make Bi_3ClO_4-based nanomaterials promising candidates for next-generation photocatalytic systems aimed at sustainable water purification.[48,49]

In this context, the present research focuses on the synthesis, characterization, and application of Bi_3ClO_4 nanomaterials for efficient dye degradation. Understanding the structure–property–performance relationship of such nanocatalysts is essential for optimizing their photocatalytic activity and advancing their practical implementation in environmental remediation technologies.

2 Materials and methods

2.1 Chemicals

All chemicals used were of analytical reagent (AR) grade, including bismuth nitrate ($Bi(NO_3)_3$; Sigma-Aldrich, 98% purity), potassium chloride (KCl; Sigma-Aldrich), and formaldehyde (HCHO). Potassium hydroxide (KOH) was used to adjust the pH. The model dyes, crystal violet (CV) and methylene blue (MB), were obtained from E. Merck, India, and used without further purification. Double-distilled water (DDW) was used throughout the experiments.

2.2 Synthesis of Bi_3ClO_4 nanoparticles

Bismuth oxychloride (Bi_3ClO_4) was synthesized using a co-precipitation method. Double-distilled water (DDW) was used as the solvent in synthesis and electrochemical studies. In a typical procedure, 0.485 g of bismuth nitrate ($Bi(NO_3)_3$) was dissolved in 10 mL of formaldehyde and stirred vigorously for 30 minutes. After this, 4 M KOH and 2 M KCl were added separately to the solution. The mixture was then stirred for another 30 minutes, during which a white suspension formed, indicating product formation. The resulting precipitate was washed several times with DDW and ethanol to remove impurities and then dried at 100 °C for 6 hours.

3 Characterization

3.1 Materials characterization

Cu Kα radiation (λ = 1.5406 Å) was used to obtain X-ray diffraction (XRD) patterns on a Rigaku D/Max-TTR III X-ray diffractometer in the 2θ range from 5° to 90°. This method was used to ascertain the synthesised material's phase composition and crystalline structure. A Renishaw Raman spectrometer was used to perform Raman spectroscopy measurements, which allowed for the identification of the sample's vibrational modes and chemical bonding information. Field-emission scanning electron microscopy (FE-SEM) on a JEOL JSM-6701F instrument was used to characterise the material's surface morphology. This method provided high-resolution images to

© 2026 The Author(s). Published by the Royal Society of Chemistry

Open Access Article. Published on 23 March 2026. Downloaded on 4/30/2026 8:36:08 PM.
This article is licensed under a Creative Commons Attribution-NonCommercial 3.0 Unported Licence.

study the particle size, shape, and surface characteristics of materials. The specific surface area and pore properties of the material were ascertained by measuring adsorption and desorption isotherms using a BET flowing gas surface area analyser.

3.2 Photocatalytic activity

The photocatalytic activity of Bi_3ClO_4 nanoparticles for the degradation of crystal violet (CV) and methylene blue (MB) dyes was evaluated under natural sunlight. This was accomplished by dispersing 10 mg of Bi_3ClO_4 nanoparticles in 100 mL of a 10 ppm CV or the MB dye solution. The suspension was magnetically stirred for 60 min in the dark to reach the adsorption equilibrium. To avoid localized overheating, the reaction vessel was kept in a water bath under open-atmospheric conditions with continuous magnetic stirring. Hence, the solution temperature was kept in the range from 27 °C to 30 °C during irradiation. Dark control experiments confirmed negligible dye degradation, indicating that the removal process was predominantly photocatalytic rather than thermally driven. Every 15 minutes, 10 mL of this solution was collected. The solution was centrifuged to extract the Bi_3ClO_4 nanoparticles, and the concentration of CV or the MB dye was detected using a UV-visible spectrometer.

4 Results and discussion

4.1 Physicochemical characterizations

4.1.1 X-ray diffraction (XRD) of the as-synthesized photocatalyst. The recorded diffraction pattern agrees well with the standard reference data (PDF no. 00-036-0760), confirming the successful formation of monoclinic Bi_3ClO_4.[50] The XRD pattern exhibits sharp, well-defined peaks at 2θ values of approximately 9.49°, 19.08°, 21.80°, 22.18°, 23.98°, 28.77°, 29.13°, 31.40°, 31.64°, 37.97°, 38.77°, 43.36°, 45.25°, 46.56°, 50.10°, 52.07°, and 54.85°, indicating the good crystallinity of the prepared sample. These diffraction peaks can be indexed to the (200), (400), (310), (011), (211), (600), (411), (002), (020), (3$\bar{1}$2), (800), (620), (022), (222), (721), (213), and (431) crystal planes of monoclinic Bi_3ClO_4, respectively, which further validates the phase purity of the synthesized material. No additional impurity peaks were detected, suggesting the formation of single-phase Bi_3ClO_4, as illustrated in Fig. 1a. The relatively narrow peak widths indicate the formation of nanosized crystallites; the average crystallite size can be estimated using the Debye–Scherrer equation, which typically falls in the nanometer range for such systems, supporting the nanoscale nature of the material. The high crystallinity and phase purity revealed by XRD are expected to enhance the separation and transport of photogenerated charge carriers, thereby contributing to improved photocatalytic performance under visible-light irradiation.

The average crystallite size of Bi_3ClO_4 was estimated using the Scherrer equation:[51]

$$D = K\lambda/\beta \cos\theta \quad (1)$$

where D represents the crystallite size, K is the shape factor (0.94), β is the full width at half-maximum (FWHM) of the diffraction peak, θ is the Bragg angle, and λ is the wavelength of the X-ray source (0.15406 nm). Based on this calculation, the average crystallite size of the synthesized Bi_3ClO_4 is found to be approximately 5.6 nm. The crystallite size calculated using the Scherrer equation from the (200) diffraction peak at $2\theta \approx 9.5°$ was found to be of approximately 5.6 nm. This value represents the size of coherent diffraction domains rather than the actual particle dimensions. The larger nanosheet-like structures observed in SEM images (Fig. 4a (50–100 nm)) are likely formed *via* the aggregation of several smaller crystallites during the growth process.

4.1.2 Raman spectroscopic analysis. Raman spectroscopy was employed to further examine the structural order and vibrational characteristics of the synthesized Bi_3ClO_4

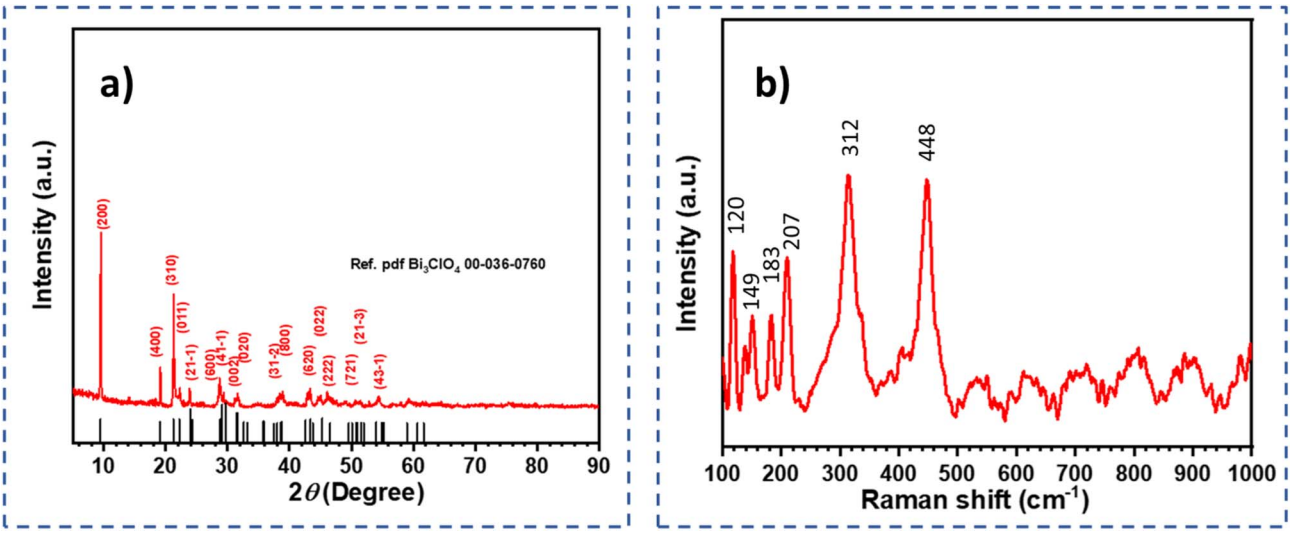

Fig. 1 (a) X-ray diffraction pattern of Bi_3ClO_4. (b) Raman spectrum of Bi_3ClO_4.

Open Access Article. Published on 23 March 2026. Downloaded on 4/30/2026 8:36:08 PM. This article is licensed under a Creative Commons Attribution-NonCommercial 3.0 Unported Licence.

nanoparticles, and the corresponding spectrum is presented in Fig. 1b. Several distinct Raman bands are observed at approximately 120, 149, 183, 207, 312, and 448 cm^{-1}, which are consistent with previously reported vibrational modes of monoclinic Bi_3ClO_4.[52–54] The low-frequency bands in the range of 100–220 cm^{-1} are mainly associated with lattice vibrations and external Bi–Cl stretching modes with the A_{1g} symmetry, arising from the motion of Bi^{3+} ions against the surrounding Cl^- framework. The bands located at ~183 and 207 cm^{-1} can be attributed to internal Bi–Cl stretching and bending vibrations corresponding to the A_{1g} and E_g modes of the distorted Bi–Cl polyhedron, respectively. The higher-frequency bands at ~312 and 448 cm^{-1} are assigned to the symmetric and asymmetric stretching vibrations of Bi–Cl bonds within the Bi_3ClO_4 lattice, respectively, indicating the presence of well-defined Bi–Cl coordination environments. The relatively sharp and well-resolved Raman peaks suggest the good crystallinity and structural ordering of the synthesized nanoparticles, which is in agreement with the XRD results. Moreover, the absence of additional Raman bands corresponding to possible impurity phases, such as Bi_2O_3 or BiOCl, further confirms the phase purity of the prepared sample. The slight peak broadening observed in the spectrum may be attributed to the nanoscale crystallite size and lattice strain effects commonly present in nanostructured materials. Such structural features can influence phonon confinement and defect density, which in turn affect charge carrier dynamics during photocatalysis. Therefore, the Raman results, together with XRD analysis, confirm the successful formation of crystalline and phase-pure Bi_3ClO_4 with a well-defined monoclinic structure, which is expected to be beneficial for enhanced photocatalytic activity under visible-light irradiation.

4.1.3 UV-vis absorption analysis of Bi_3ClO_4. Ultraviolet (UV) spectroscopy is a widely used analytical technique for investigating the optical properties and electronic structure of materials. It is based on the absorption of ultraviolet or visible radiation by a substance, resulting in electronic transitions between molecular orbitals. The UV-vis absorption spectrum of Bi_3ClO_4 (Fig. 2a) exhibits a strong optical absorption in the 420–800 nm wavelength range, indicating that Bi_3ClO_4 can efficiently absorb visible light and acts as a solar-light-driven active photocatalyst for dye degradation. The valence band (VB) and conduction band (CB) of Bi_3ClO_4 are poised by hybridized Bi 6s/O 2p orbitals and Cl 3d orbitals, respectively. The band gap and absorption coefficient, according to the Kubelka–Munk equation, can be expressed as $\alpha h\nu = A(h\nu - E_g)^{1/2}$, where α, ν and h represent the absorption coefficient, the frequency of light and Planck's constant, respectively. The Tauc plot (Fig. 2b), constructed by plotting $(\alpha h\nu)^2$ *versus* photon energy ($h\nu$), was used to determine the band gap energy. The intercept of the tangent at the x-axis is a good estimate of the band gap E_g. For the prepared Bi_3ClO_4 nanoparticles, a band gap of 2.67 eV is observed. The E_g value decreases as the crystallite size increases. The band gap of a material is affected by the size of the particles and its crystal structure.

4.1.4 Brunauer–Emmett–Teller (BET) surface area analysis. It is widely recognized that a higher specific surface area in electrode materials leads to an increased number of accessible active sites, which in turn facilitates charge transfer processes. The textural properties of Bi_3ClO_4 were evaluated through nitrogen adsorption–desorption measurements. As shown in Fig. 3a, the adsorption isotherms exhibit a type-III profile accompanied by an H3 hysteresis loop in the relative pressure (P/P_0) range of 0.45–1.0, indicating the presence of microporous features.[55]

The pore size distribution curve, derived from the Barrett–Joyner–Halenda (BJH) model (Fig. 3b), shows that the material possesses a broad pore size distribution in the mesoporous region, confirming the formation of a hierarchical porous structure. The Brunauer–Emmett–Teller (BET) specific surface area of Bi_3ClO_4 is calculated to be 13.68 $m^2\ g^{-1}$. This surface area is moderate due to the stacking of nanosheets, which reduces the accessible surface area but still exposes active edge sites. Several studies on BiOCl nanosheets have reported

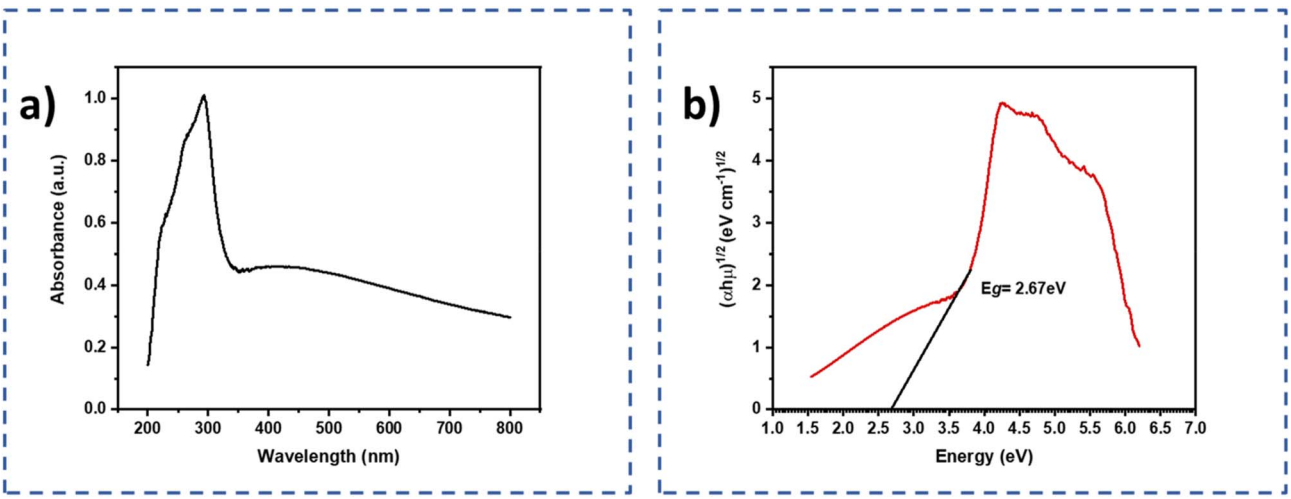

Fig. 2 (a) UV-vis absorption spectrum and (b) Tauc plot ($(\alpha h\nu)^2$ *vs.* photon energy (eV)) of the Bi_3ClO_4 photocatalyst.

© 2026 The Author(s). Published by the Royal Society of Chemistry

Open Access Article. Published on 23 March 2026. Downloaded on 4/30/2026 8:36:08 PM.
This article is licensed under a Creative Commons Attribution-NonCommercial 3.0 Unported Licence.

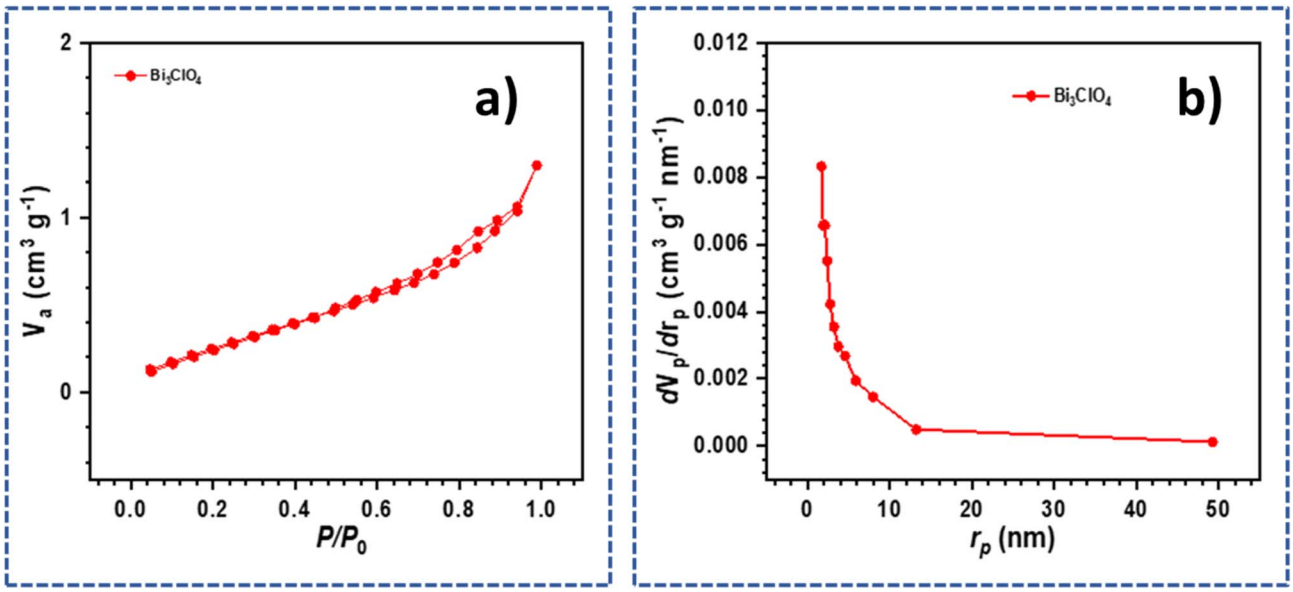

Fig. 3 (a) N_2 adsorption isotherm and (b) pore size variation of Bi_3ClO_4.

comparable or even lower values. For instance, P–BiOCl nanosheets exhibit a surface area of 13.4 m^2 g^{-1},[56] while hierarchical BiOCl structures show values as low as 7.3 m^2 g^{-1} (ref. 57) and even 3.49 m^2 g^{-1}, depending on the morphology and stacking of nanosheets.[58] Therefore, the obtained surface area of bismuth-based photocatalysts indicates the formation of nano-sized particles with accessible surface sites.[59] The presence of mesopores and interparticle voids can significantly enhance the mass transport of dye molecules and provide more adsorption sites for photocatalytic reactions. Furthermore, the mean pore radius remains nearly unchanged, suggesting that the observed increase in the surface area is mainly due to particle size reduction, improved dispersion, and structural reorganization rather than the creation of new pore channels. The enhanced surface area and mesoporous architecture are expected to play an important role in improving photocatalytic performance by providing more active reaction sites, shortening charge-carrier diffusion pathways, and facilitating the adsorption of organic dye molecules on the catalyst surface. In addition, the porous structure can promote light harvesting *via* multiple scattering within the pores, thereby increasing the probability of photon absorption. These combined structural and textural advantages are beneficial for the efficient separation and transfer of photogenerated electron–hole pairs, ultimately contributing to the improved photocatalytic activity of Bi_3ClO_4 under visible-light irradiation.[60]

4.1.5 Field-emission scanning electron microscopy analysis (FE-SEM). The surface morphology and microstructural characteristics of the synthesized Bi_3ClO_4 sample were thoroughly examined using field-emission scanning electron microscopy (FESEM), and the representative images are displayed in Fig. 4a–d. The low-magnification FESEM image (Fig. 4a) reveals that the Bi_3ClO_4 sample is composed of densely packed, irregularly arranged petal-like structures forming a hierarchical assembly. These structures appear to be loosely stacked and interconnected, producing a three-dimensional architecture with numerous open spaces and channels. Such a morphology indicates that the growth process favours anisotropic crystal formation, leading to the development of layered units that aggregate into larger clusters. A closer inspection at higher magnification (Fig. 4b) clearly shows that the material is constructed from ultrathin nanosheets that are curled, folded, and randomly oriented. These nanosheets resemble the natural petal-like structure of water hyacinth leaves (Fig. 4c), forming a flower-like or lamellar architecture. The sheets are not perfectly flat; instead, they exhibit bending, wrinkling, and edge curling, which suggests a very low thickness and high flexibility. The lateral size of these nanosheets typically ranges from 50 to 100 nm, while their thickness remains in the 5–10 nm scale. The interweaving of such thin sheets generates a porous framework with abundant voids between adjacent layers. This open and hierarchical nanosheet assembly is advantageous because it provides a large accessible surface area, promotes effective light scattering within the structure, and facilitates rapid diffusion of reactant molecules during photocatalytic processes. In the petal-like arrangement of the nanosheets, individual sheets overlap and radiate outward in a manner similar to the natural water hyacinth (*Eichhornia crassipes*) plant's leaves. This biomimetic morphology significantly increases the density of exposed edge sites, surface defects, and unsaturated coordination centers. These features are particularly beneficial for photocatalytic applications, as they can serve as active sites for adsorption and surface reactions. In addition, the intimate contact between adjacent nanosheets is expected to provide efficient pathways for charge transport, thereby reducing the recombination probability of photogenerated electron–hole pairs. The hierarchical stacking and porous arrangement also enhance photon harvesting by allowing multiple internal reflections of incident light, ultimately improving the photocatalytic efficiency of the Bi_3ClO_4 material.

Open Access Article. Published on 23 March 2026. Downloaded on 4/30/2026 8:36:08 PM.
This article is licensed under a Creative Commons Attribution-NonCommercial 3.0 Unported Licence.

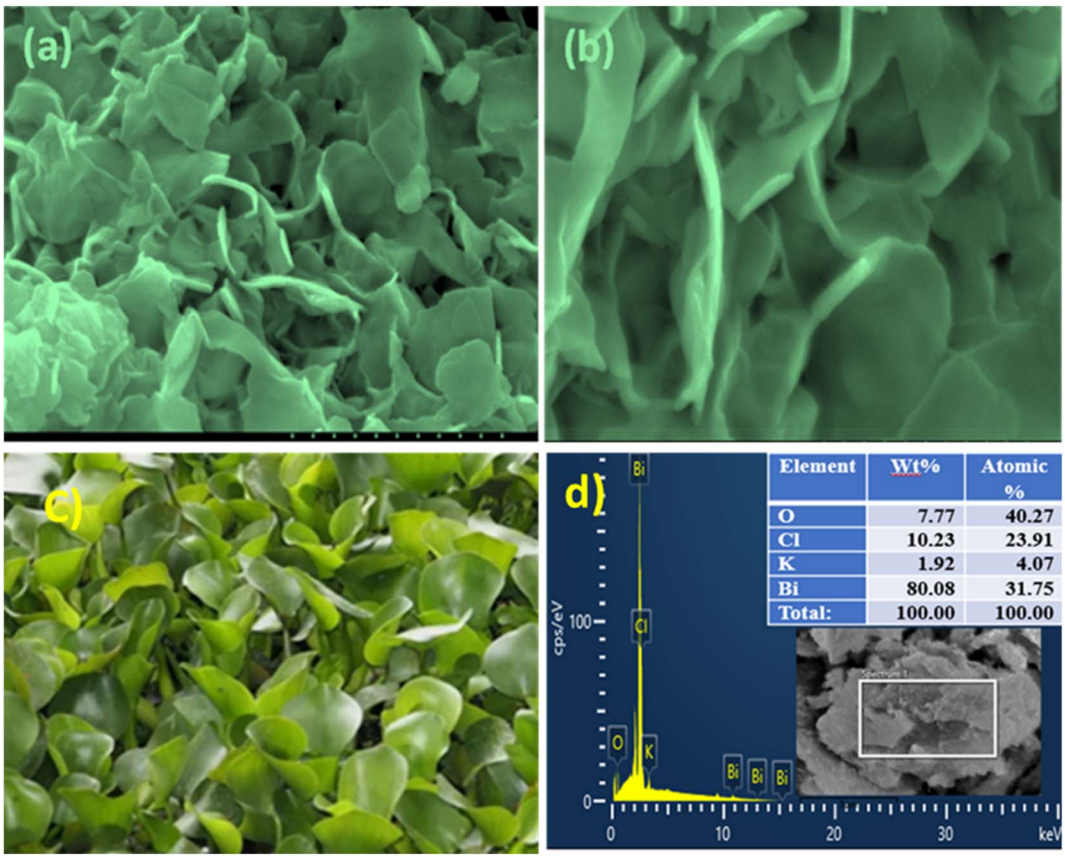

Fig. 4 (a and b) SEM images of Bi_3ClO_4; (c) photograph of water hyacinth leaves (*Eichhornia crassipes*); (d) EDS spectrum of Bi_3ClO_4, with inset showing the corresponding SEM image of the selected area.

The elemental composition and chemical purity of the Bi_3ClO_4 sample were analyzed by energy-dispersive X-ray spectroscopy (EDS), as presented in Fig. 4d. The EDS spectrum confirms the presence of Bi, O, and Cl as the primary elements, which is consistent with the expected composition of Bi_3ClO_4. A small signal corresponding to K is also observed, which may originate from residual precursor salts or synthesis-related additives. The quantitative analysis indicates that Bi is the dominant element, accounting for the majority of the weight percentage, while oxygen and chlorine are present in appropriate proportions to form the oxychloride structure. The absence of any additional impurity peaks suggests that the synthesized sample possesses high chemical purity. Furthermore, the inset of the mapping region demonstrates that the elements are uniformly distributed throughout the selected area, confirming compositional homogeneity at the microscale.

Overall, the FESEM and EDS analyses reveal that the synthesized Bi_3ClO_4 exhibits a well-defined hierarchical nanosheet-assembled morphology resembling water-hyacinth-like petals. This unique architecture provides several structural advantages, including a high specific surface area, abundant exposed active sites, improved light-harvesting capability, and efficient charge-transfer pathways. Such morphological and compositional features are expected to play a crucial role in enhancing the photocatalytic activity and overall functional performance of the Bi_3ClO_4 material under visible-light irradiation.

4.2 Photocatalytic degradation of the CV dye

The photodegradation of crystal violet (CV) was examined, and additional studies on the degradation of organic dyes over Bi_3ClO_4 were performed under UV and visible-light irradiation. Crystal violet was chosen as one of the additional contaminants among various anionic dye types. A blank test was also done to make sure the dye was not photodegrading on its own. Excellent visible-light photocatalytic activity is demonstrated by Bi_3ClO_4, and it requires only 75 minutes to completely break down different contaminants. Under visible-light illumination, the photocatalytic degradation rates of pollutants were still higher than those under UV-light illumination, as shown in Fig. 5a–c. The photocatalytic activity of Bi_3ClO_4 was tested for degrading the CV dye under visible-light irradiation, and the results are displayed in Fig. 5b. It can be seen that under dark conditions, only negligible amounts of CV are degraded. In contrast to the dark condition, the degradation activity under the light irradiation is extremely enhanced, achieving an approximately 100% degradation efficiency within 75 min in the presence of the Bi_3ClO_4 photocatalyst. Fig. 5c shows the rate constant of the photocatalytic reaction, calculated from the slope of the plot of $\ln(C_0/C_t)$ *versus* irradiation time, where C_0 is the initial CV

© 2026 The Author(s). Published by the Royal Society of Chemistry

Open Access Article. Published on 23 March 2026. Downloaded on 4/30/2026 8:36:08 PM.
This article is licensed under a Creative Commons Attribution-NonCommercial 3.0 Unported Licence.

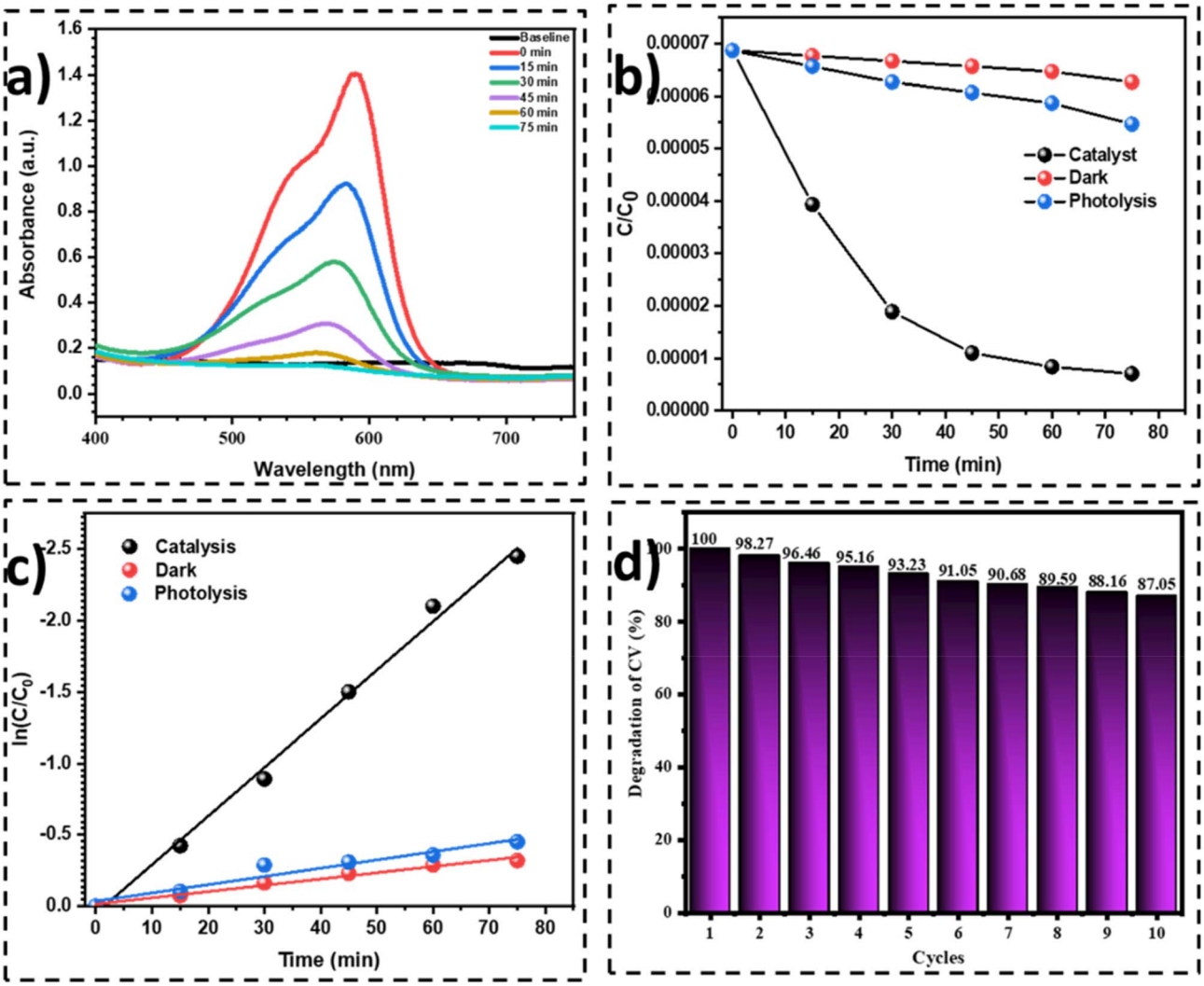

Fig. 5 (a) UV-visible spectra of the photocatalytic degradation of the CV dye, (b) time-evolved photocatalytic degradation of CV under visible light irradiation, (c) rate of chemical kinetics of the Bi_3ClO_4 NPs during photocatalytic CV degradation, and (d) bar chart of the reusability test of Bi_3ClO_4 NPs for the CV dye degradation.

concentration and C_t is the concentration of CV at time t. Therefore, the slope of the $\ln(C/C_0)$ *vs.* t curve may be used to determine the rate constant k, which is 0.050 min^{-1}, indicating that the Bi_3ClO_4 photocatalyst's ability to degrade the CV dye improved when exposed to visible light. The stability and reusability of the photocatalyst were assessed over ten successive photocatalytic cycles during the regeneration process (Fig. 5d). After each cycle, the synthesized photocatalyst was washed with room-temperature distilled water and ethanol and then dried at 60 °C to avoid any possible structural or surface modification. The degrading efficiency of crystal violet decreased from 100% to 87.05% after 10 cycles, which is a small 12.95% decrease. The result suggests that the produced catalysts have superior chemical stability and can potentially be recycled during the purification of wastewater containing organic colours. According to the Langmuir–Hinshelwood model, the photocatalytic degradation of organic substrates generally follows pseudo-first-order kinetics at low concentrations. Under such conditions, the reaction rate can be expressed as a function of the pollutant concentration.[61] The stated pseudo-first-order equation is as follows:

$$\ln\left(\frac{C}{C_0}\right) = -kt. \quad (2)$$

The photocatalytic kinetics were analysed using the Langmuir–Hinshelwood pseudo-first-order model, expressed as $\ln(C_0/C_t)$ *versus* time. The reaction rate constant (k) was determined from the slope of the linear plot. As shown in Fig. 5c, a strong linear relationship between $\ln(C_0/C_t)$ and time (t) was observed for Bi_3ClO_4 during the reaction stage ($R^2 = 0.9931$), whereas photolysis and dark conditions exhibited lower linearity with R^2 values of 0.97476 and 0.92056, respectively.

4.3 Photocatalytic degradation of the MB dye

Visible light was used for the degradation of methylene blue (MB) in the presence of the Bi_3ClO_4 catalyst. Among the

Open Access Article. Published on 23 March 2026. Downloaded on 4/30/2026 8:36:08 PM. This article is licensed under a Creative Commons Attribution-NonCommercial 3.0 Unported Licence.

different kinds of anionic dyes, MB was selected as one of the extra pollutants. The examination of Bi_3ClO_4's photocatalytic activity for the MB dye degradation under visible light irradiation is presented in Fig. 6a–c. Bi_3ClO_4 showed excellent visible-light photocatalytic activity, and it took only 105 minutes to fully degrade pollutants. As seen in Fig. 6a, the photocatalytic degradation rates of contaminants under visible light irradiation were still higher than those under UV light illumination. Within 105 minutes, the Bi_3ClO_4 disintegration rate reached 96% due to the acceptance of the electrons produced by the Bi_3ClO_4 particles, which inhibits the production of charges. Under dark conditions, only negligible amounts of MB were degraded. In contrast to the dark condition, the degradation activity was extremely enhanced under light irradiation, achieving an approximately 96% degradation efficiency in the presence of the Bi_3ClO_4 photocatalyst. The results are shown in Fig. 6b. The durability of the Bi_3ClO_4 photocatalyst was investigated through ten repeated photocatalytic cycles, demonstrating its stability during the regeneration process (Fig. 6d). After ten cycles, the degradation efficiency of methylene blue dropped by 9%, from 96% to 87%. The outcome indicated that the generated catalysts had better chemical stability and could be recycled to purify wastewater containing organic colours. The dependency of the photocatalytic reaction rate on the organic pollutant concentration at low substrate concentrations could be represented using a pseudo-first-order equation. As shown in Fig. 6c, a linear relationship between $\ln(C_0/C_t)$ and time (t) was observed for Bi_3ClO_4 during the reaction stage ($R^2 = 0.9097$), while photolysis and dark conditions exhibited R^2 values of 0.97631 and 0.78367, respectively. The reaction rate constant (k) was determined from the slope of the $\ln(C_0/C_t)$ *versus* time plot, yielding a value of 0.054 min^{-1} for Bi_3ClO_4.

4.4 Reactive species capturing experiment

The scavenger-based trapping experiments were carried out to identify the main reactive species. Ethylenediaminetetraacetic acid (EDTA), *p*-benzoquinone (BQ), sodium azide (NaN_3), and isopropyl alcohol (IPA) were used as scavengers for

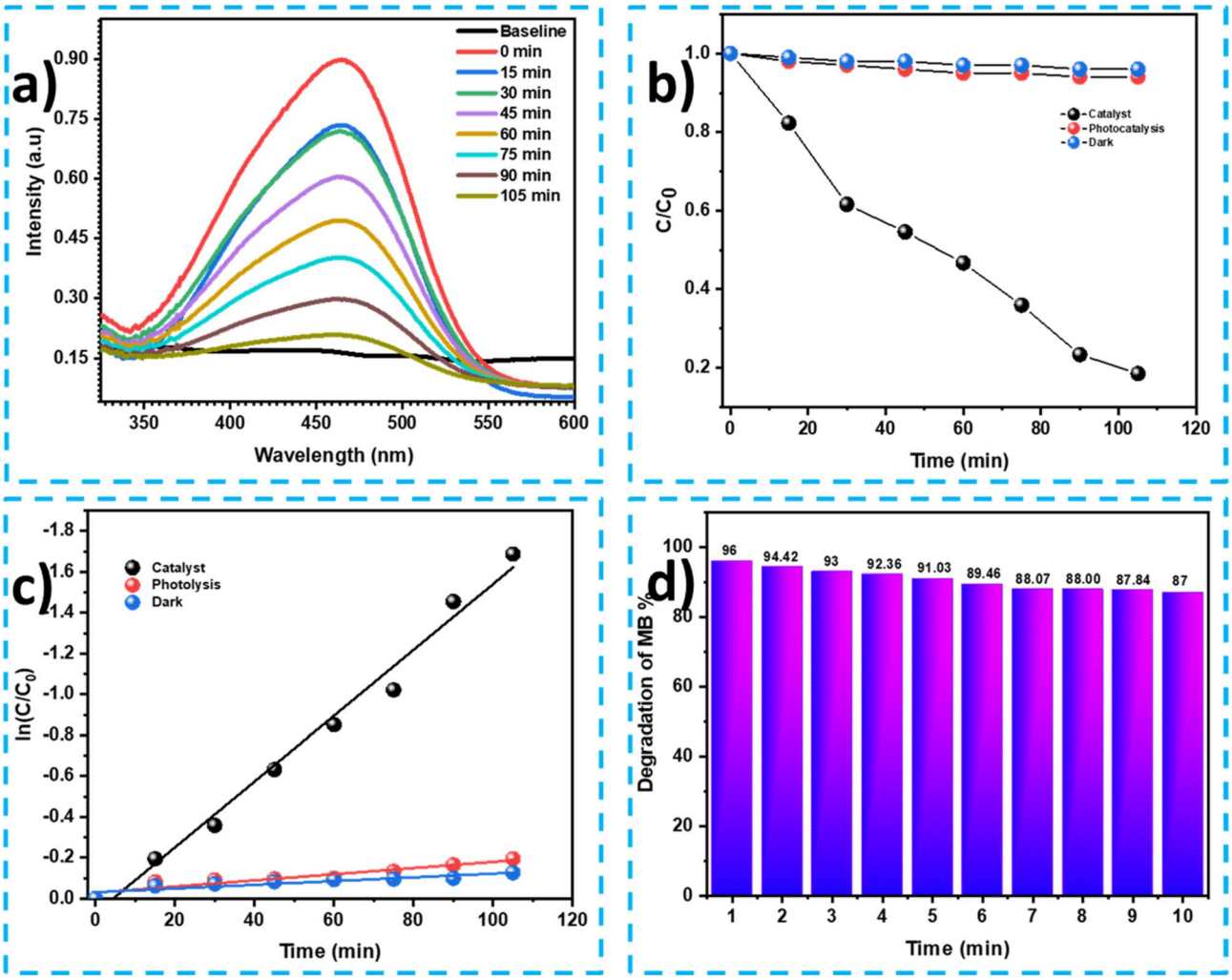

Fig. 6 (a) UV-visible spectra of the photocatalytic degradation of the MB dye, (b) time-evolved photocatalytic degradation of MB under visible light irradiation, (c) first-order kinetics of the photodegradation of the MB dye on Bi_3ClO_4, and (d) bar chart of the reusability test of Bi_3ClO_4 NPs for the MB dye degradation.

© 2026 The Author(s). Published by the Royal Society of Chemistry

Open Access Article. Published on 23 March 2026. Downloaded on 4/30/2026 8:36:08 PM.
This article is licensed under a Creative Commons Attribution-NonCommercial 3.0 Unported Licence.

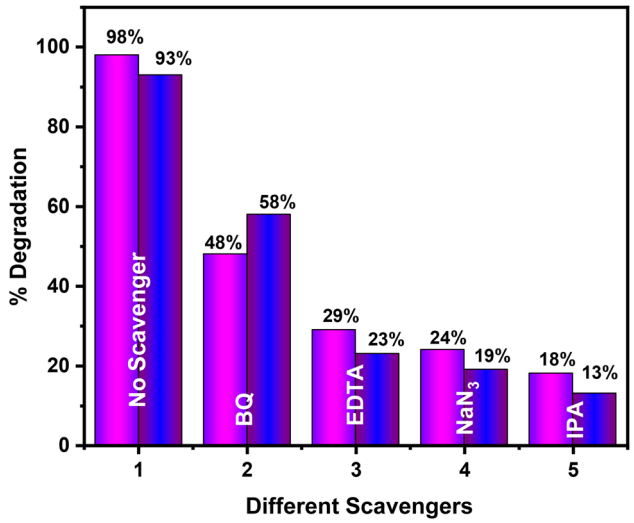

Fig. 7 Photocatalytic degradation efficiency of Bi_3ClO_4 under sunlight irradiation in the presence of different scavengers: BQ ($O_2^{\bullet-}$), EDTA (h^+), NaN_3 ($^1O_2$), and IPA ($^\bullet OH$).

photogenerated holes (h^+), superoxide radicals ($O_2^{\bullet-}$), singlet oxygen ($^1O_2$), and hydroxyl radicals ($^\bullet OH$), respectively. In each experiment, 10 mL of 0.1 mol L^{-1} solutions of EDTA, BQ, NaN_3, and IPA was added separately to crystal violet (CV) and methylene blue (MB) dye solutions.

The role of reactive species in the photocatalytic degradation process was investigated using various scavengers under sunlight irradiation (Fig. 7). The photogenerated holes (h^+) was evaluated using EDTA as a hole quencher. During CV degradation, the presence of EDTA results in only a slight reduction in removal efficiency, implying that holes contribute marginally to the oxidation process. In contrast, a substantial decline in MB degradation was observed upon EDTA addition, indicating that photogenerated holes play a significant role in the degradation pathway of MB. The involvement of singlet oxygen ($^1O_2$) was examined using sodium azide (NaN_3). The pronounced suppression of MB degradation in the presence of NaN_3 confirms that singlet oxygen acts as a major reactive species in MB decomposition. However, its effect during CV degradation is comparatively minor, revealing only a secondary contribution. Notably, the addition of isopropanol (IPA), a well-known hydroxyl radical ($^\bullet OH$) scavenger, leads to a dramatic decrease in the degradation efficiencies of both CV and MB. This strong inhibitory effect demonstrates that hydroxyl radicals are the predominant reactive oxygen species governing the photocatalytic degradation of both dyes. The proposed photocatalytic reaction pathways are outlined in eqn (3)–(9).

4.5 Reaction mechanisms of the Bi_3ClO_4 photocatalyst for the removal of organic dyes

$$Bi_3ClO_4 + h\nu \rightarrow Bi_3ClO_4 (e_{CB}^- + h_{VB}^+) \quad (3)$$

$$Bi_3ClO_4 (h_{VB}^+) + H_2O \rightarrow Bi_3ClO_4 + H^+ + OH^\bullet \quad (4)$$

$$Bi_3ClO_4 (h_{VB}^+) + OH^- \rightarrow Bi_3ClO_4 + OH^\bullet \quad (5)$$

$$Bi_3ClO_4 (e_{CB}^-) + O_2 \rightarrow Bi_3ClO_4 + O_2^{\bullet-} \quad (6)$$

$$O_2^{\bullet-} + H^+ \rightarrow HO_2^\bullet \quad (7)$$

$$HO_2^\bullet + HO_2^\bullet \rightarrow H_2O_2 + O_2 \quad (8)$$

$$Bi_3ClO_4 (e_{CB}^-) + H_2O_2 \rightarrow OH^- + OH^\bullet \quad (9)$$

$$\text{Organic dye} + O_2 + OH^\bullet \rightarrow H_2O + CO_2 + \text{other products}$$

A plausible photocatalytic degradation mechanism of Bi_3ClO_4 nanoparticles can be explained based on photoinduced charge generation and subsequent reactive oxygen species (ROS) formation. Upon irradiation with photons possessing energy equal to or greater than the band gap energy (E_g), Bi_3ClO_4 absorbs light and undergoes electronic excitation. Electrons from the valence band (VB) are promoted to the conduction band (CB), simultaneously generating positively charged holes (h^+) in the VB (eqn (3)). This process results in the formation of electron–hole pairs within the semiconductor matrix. Following excitation, the photogenerated charge carriers migrate toward the surface of the catalyst. The conduction band electrons interact with dissolved molecular oxygen adsorbed on the catalyst surface, leading to the formation of superoxide radical species ($O_2^{\bullet-}$) (eqn (4)–(6)). Concurrently, the valence band holes react with surface-adsorbed water molecules or hydroxide ions to generate highly oxidative hydroxyl radicals ($^\bullet OH$) (eqn (5)). The formed superoxide radicals may further participate in secondary reactions. In the presence of protons (H^+), $O_2^{\bullet-}$ can be converted into hydroperoxyl radicals ($^\bullet OOH$), which subsequently undergo disproportionation or reduction steps to produce hydrogen peroxide (H_2O_2). Hydrogen peroxide can then decompose, either photolytically or *via* electron-mediated pathways, yielding additional hydroxyl radicals ($^\bullet OH$) (eqn (7)–(9)). These reactive oxygen species, particularly hydroxyl radicals, possess strong oxidative potential and are primarily responsible for the breakdown and mineralization of organic dye molecules. The overall degradation pathway thus involves sequential charge generation, surface redox reactions, and ROS-mediated oxidation of pollutants.

Based on the active species trapping experiments and band energy level analysis, a plausible photocatalytic degradation mechanism of crystal violet (CV) and methylene blue (MB) over Bi_3ClO_4 is proposed in the Fig. 8. The trapping results reveal that the photogenerated holes (h^+) in the VB are the dominant active species responsible for the degradation of both CV and MB. These highly oxidative holes can directly oxidize dye molecules adsorbed on the catalyst surface. Meanwhile, the photoinduced electrons in the CB react with dissolved oxygen (O_2) to generate superoxide radicals ($O_2^{\bullet-}$), which further participate in the degradation process. Additionally, hydroxyl radicals ($^\bullet OH$) may be formed either *via* the oxidation of surface-adsorbed H_2O/OH^- by h^+ or through subsequent reactions involving $O_2^{\bullet-}$. Although $O_2^{\bullet-}$ and h^+ contribute to dye

Open Access Article. Published on 23 March 2026. Downloaded on 4/30/2026 8:36:08 PM.
This article is licensed under a Creative Commons Attribution-NonCommercial 3.0 Unported Licence.

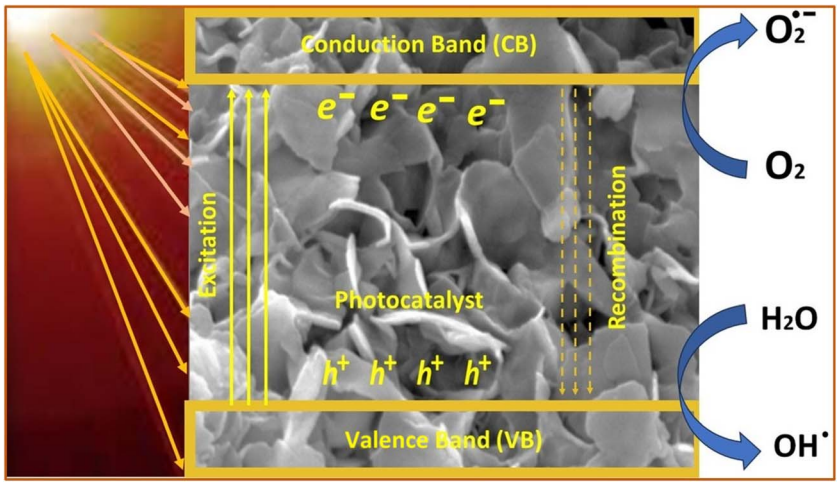

Fig. 8 Schematic of the photocatalytic production of radicals for the degradation of dyes under visible light irradiation.

decomposition, their roles are secondary compared to the direct oxidation by hydroxyl radicals (˙OH), as evidenced by the scavenger experiments. Therefore, the photocatalytic degradation of CV over Bi_3ClO_4 is primarily governed by the strong oxidative ability of hydroxyl radicals (˙OH), whereas the degradation of MB is controlled by the combined action of ˙OH, photogenerated holes (h^+), and superoxide radicals ($O_2^{\bullet -}$), enhancing the overall degradation efficiency.

5 Conclusion

In conclusion, this study successfully synthesized bismuth oxychloride (Bi_3ClO_4) nanomaterials by a co-precipitation method for the efficient photocatalytic degradation of dyes. The synthesized material has a monoclinic structure and a crystallite size of 5–6 nm. Different characterization techniques, including XRD, Raman spectroscopy, UV-visible spectroscopy, FESEM, and EDS, confirm the successful synthesis, structural integrity, elemental composition, and nanosheet-like morphology of the nanomaterials. The monoclinic bismuth oxychloride (Bi_3ClO_4) demonstrates superior performance, achieving nearly 100% degradation of crystal violet (CV) dye within 75 minutes and 96% degradation of the MB dye within 105 minutes of visible light irradiation. These remarkable results highlight the potential of the monoclinic bismuth oxychloride (Bi_3ClO_4) nanomaterial as a promising photocatalyst for environmental remediation and wastewater treatment applications.

Author contributions

Rajvardhan K. Chougale: methodology, writing – original draft, Prashant D. Sanadi: resources, Sharadchandra S. Patil: resource, Umesh S. Siddharth: resource, Pravin P. Pawar: resource, Babasaheb D. Bhosale: supervision, and Ganesh S. Kamble: methodology, supervision, project administration, validation and revision.

Conflicts of interest

There is no actual or potential conflict of interest in relation to this article.

Data availability

Original data were generated and analysed in this study. All data are provided within the manuscript.

Acknowledgements

The authors (GSK, RKC, and PDS) express their gratitude to CFC-SAIF-DST, Shivaji University Kolhapur, for the research instrument facilities. Additionally, GSK and RKC thank Chhatrapati Shahu Maharaj Research, Training and Human Development Institute (SARTHI), Pune (an autonomous institute of Government of Maharashtra), for the financial support provided under the SARATHI Fellowship-2020.

References

1 T. Robinson, G. McMullan, R. Marchant and P. Nigam, Remediation of dyes in textile effluent: a critical review on current treatment technologies with a proposed alternative, *Bioresour. Technol.*, 2001, 77, 247–255, DOI: 10.1016/s0960-8524(00)00080-8.

2 M. Kumar, A. Mishra, S. K. Patel, J. Kushwaha, S. Singh, V. Mishra, D. Singh, V. Singh, B. S. Giri, R. R. Singhania and D. Singh, Environmental Impacts and Strategies for Bioremediation of Dye-Containing Wastewater, *Bioengineering*, 2025, **12**, 1043, DOI: 10.3390/bioengineering12101043.

3 M. Farhan Hanafi and N. Sapawe, A review on the water problem associate with organic pollutants derived from phenol, methyl orange, and remazol brilliant blue dyes, *Mater. Today: Proc.*, 2020, **31**, A141–A150, DOI: 10.1016/j.matpr.2021.01.258.

© 2026 The Author(s). Published by the Royal Society of Chemistry

Open Access Article. Published on 23 March 2026. Downloaded on 4/30/2026 8:36:08 PM. This article is licensed under a Creative Commons Attribution-NonCommercial 3.0 Unported Licence.

4 G. Sriram, A. Bendre, E. Mariappan, T. Altalhi, M. Kigga, Y. C. Ching, H.-Y. Jung, B. Bhaduri and M. Kurkuri, Recent trends in the application of metal-organic frameworks (MOFs) for the removal of toxic dyes and their removal mechanism-a review, *Sustainable Mater. Technol.*, 2022, **31**, e00378, DOI: 10.1016/j.susmat.2021.e00378.

5 E. Forgacs, T. Cserháti and G. Oros, Removal of synthetic dyes from wastewaters: a review, *Environ. Int.*, 2004, **30**, 953–971, DOI: 10.1016/j.envint.2004.02.001.

6 R. Al-Tohamy, S. S. Ali, F. Li, K. M. Okasha, Y. A.-G. Mahmoud, T. Elsamahy, H. Jiao, Y. Fu and J. Sun, A critical review on the treatment of dye-containing wastewater: Ecotoxicological and health concerns of textile dyes and possible remediation approaches for environmental safety, *Ecotoxicol. Environ. Saf.*, 2022, **231**, 113160, DOI: 10.1016/j.ecoenv.2021.113160.

7 T. A. Aragaw, A review of dye biodegradation in textile wastewater, challenges due to wastewater characteristics, and the potential of alkaliphiles, *J. Hazard. Mater. Adv.*, 2024, **16**, 100493, DOI: 10.1016/j.hazadv.2024.100493.

8 S. Khan, T. Noor, N. Iqbal and L. Yaqoob, Photocatalytic Dye Degradation from Textile Wastewater: A Review, *ACS Omega*, 2024, **9**, 21751–21767, DOI: 10.1021/acsomega.4c00887.

9 W. Wimolwattanapun, P. K. Hopke and P. Pongkiatkul, Source apportionment and potential source locations of $PM_{2.5}$ and $PM_{2.5-10}$ at residential sites in metropolitan Bangkok, *Atmos. Pollut. Res.*, 2011, **2**, 172–181, DOI: 10.5094/apr.2011.022.

10 S. El Meziani, H. Agnaou, H. El Haddaj, W. Boumya, N. Barka and A. Elhalil, Sustainable adsorption technologies for textile dye removal: Advances in biomass-derived and magnetically modified activated carbons, *Cleaner Chem. Eng.*, 2025, **12**, 100210, DOI: 10.1016/j.clce.2025.100210.

11 A. P. Periyasamy, Recent Advances in the Remediation of Textile-Dye-Containing Wastewater: Prioritizing Human Health and Sustainable Wastewater Treatment, *Sustainability*, 2024, **16**, 495, DOI: 10.3390/su16020495.

12 S. Velusamy, A. Roy, S. Sundaram and T. Kumar, A Review on Heavy Metal Ions and Containing Dyes Removal Through Graphene Oxide-Based Adsorption Strategies for Textile Wastewater Treatment, *Chem. Rec.*, 2021, 1570–1610, DOI: 10.1002/tcr.202000153.

13 M. Pera-Titus, V. García-Molina, M. A. Baños, J. Giménez and S. Esplugas, Degradation of chlorophenols by means of advanced oxidation processes: a general review, *Appl. Catal., B*, 2004, **47**, 219–256, DOI: 10.1016/j.apcatb.2003.09.010.

14 K. Lata, B. Ambade, A. Kumar and S. Gautam, Sustainable Solutions: Reviewing the Future of Textile Dye Contaminant Removal with Emerging Biological Treatments, *Limnol. Rev.*, 2024, **24**, 126–149, DOI: 10.3390/limnolrev24020007.

15 K. Hikmat, H. Aziz and F. S. Mustafa, Pharmaceutical pollution in the aquatic environment: advanced oxidation processes as efficient treatment approaches: a review, *Mater. Adv.*, 2025, 3433–3454, DOI: 10.1039/d4ma01122h.

16 P. O. Oladoye, M. Kadhom, I. Khan, K. H. Hama Aziz and Y. A. Alli, Advancements in adsorption and photodegradation technologies for Rhodamine B dye wastewater treatment: fundamentals, applications, and future directions, *Green Chem. Eng.*, 2024, **5**, 440–460, DOI: 10.1016/j.gce.2023.12.004.

17 A. Fujishima, X. Zhang and D. A. Tryk, TiO_2 photocatalysis and related surface phenomena, *Surf. Sci. Rep.*, 2008, **63**, 515–582, DOI: 10.1016/j.surfrep.2008.10.001.

18 H. Shukla, R. Gautam, Sushma and N. Kumari, A comprehensive review: Photodegradation of dyes with rare earth doped metal oxide nanoparticles for wastewater treatment, *J. Phys. Chem. Solids*, 2025, **200**, 112593, DOI: 10.1016/j.jpcs.2025.112593.

19 N. Ramesh, C. W. Lai, M. R. Bin Johan, S. M. Mousavi, I. A. Badruddin, A. Kumar, G. Sharma and F. Gapsari, Progress in photocatalytic degradation of industrial organic dye by utilising the silver doped titanium dioxide nanocomposite, *Heliyon*, 2024, **10**, e40998, DOI: 10.1016/j.heliyon.2024.e40998.

20 N. H. S. Suhaimi, R. Azhar, N. S. Adzis, M. A. Mohd Ishak, M. Z. Ramli, M. Y. Hamzah, K. Ismail and W. I. Nawawi, Recent updates on TiO_2-based materials for various photocatalytic applications in environmental remediation and energy production, *Desalin. Water Treat.*, 2025, **321**, 100976, DOI: 10.1016/j.dwt.2024.100976.

21 Q. Zhang, I. Lee, J. B. Joo, F. Zaera and Y. Yin, Core–Shell Nanostructured Catalysts, *Acc. Chem. Res.*, 2013, **46**, 1816–1824, DOI: 10.1021/ar300230s.

22 X. Wei, U. Akbar and A. Raza, A review on bismuth oxyhalide based materials for photocatalysis, *Nanoscale Adv.*, 2021, 3353–3372, DOI: 10.1039/d1na00223f.

23 X. Wei, M. U. Akbar, A. Raza and G. Li, A review on bismuth oxyhalide based materials for photocatalysis, *Nanoscale Adv.*, 2021, **3**, 3353–3372, DOI: 10.1039/d1na00223f.

24 J. Li, Y. Yu and L. Zhang, Bismuth oxyhalide nanomaterials: layered structures meet photocatalysis, *Nanoscale*, 2014, **6**, 8473–8488, DOI: 10.1039/c4nr02553a.

25 C.-C. Chen, S.-H. Chang, J. Shaya, F.-Y. Liu, Y.-Y. Lin, L.-G. Wang, H.-Y. Tsai and C.-S. Lu, Hydrothermal synthesis of BiOxBry/BiOmIn/GO composites with visible-light photocatalytic activity, *J. Taiwan Inst. Chem. Eng.*, 2022, **133**, 104272, DOI: 10.1016/j.jtice.2022.104272.

26 Q.-Q. Liu, X.-J. Weng and K.-F. Yue, Metal-induced assembly of three novel MOFs: Displaying the sensitive fluorescence sensing and rapid dye adsorption properties, *J. Solid State Chem.*, 2019, **279**, 120933, DOI: 10.1016/j.jssc.2019.120933.

27 L. Wang, Y. Liu, G. Chen, M. Zhang, X. Yang, R. Chen and Y. Cheng, Bismuth Oxychloride Nanomaterials Fighting for Human Health: From Photodegradation to Biomedical Applications, *Crystals*, 2022, **12**, 491, DOI: 10.3390/cryst12040491.

28 G. X. Castillo-Cabrera, P. Espinoza-Montero, P. Alulema-Pullupaxi, J. Mora and M. Villacís-García, Bismuth Oxyhalide-Based Materials (BiOX: X = Cl, Br, I) and Their Application in Photoelectrocatalytic Degradation of

Open Access Article. Published on 23 March 2026. Downloaded on 4/30/2026 8:36:08 PM. This article is licensed under a Creative Commons Attribution-NonCommercial 3.0 Unported Licence.

Organic Pollutants in Water: A Review, *Front. Chem.*, 2022, **10**, 9006622, DOI: 10.3389/fchem.2022.900622.

29 E. Valadez-Renteria, M. Rosales, P. C. H.-D. Castillo, C. Rodriguez-Gonzalez, T. A. Esquivel-Castro, V. Alonso, P. Salas and J. Oliva, Rubber/BiOCl:Yb,Er composite for the enhanced degradation of methylene blue and Rhodamine B dyes under solar irradiation, *J. Alloys Compd.*, 2025, **1027**, 180625, DOI: 10.1016/j.jallcom.2025.180625.

30 V. Ruiz-Santoyo, S. García-Carvajal and M. C. Arenas-Arrocena, Photocatalytic removal of synthetic dyes using Bi_2O_3–TiO_2 nanocomposites obtained by simple hydrothermal route, *J. Nanopart. Res.*, 2025, **27**, 23, DOI: 10.1007/s11051-024-06207-9.

31 K. Mahalakshmi, R. Ranjith, P. Thangavelu, M. Priyadharshini, B. Palanivel, M. A. Manthrammel, M. Shkir and B. Diravidamani, Augmenting the Photocatalytic Performance of Direct Z-Scheme Bi_2O_3/g-C_3N_4 Nanocomposite, *Catalysts*, 2022, **12**, 1544, DOI: 10.3390/catal12121544.

32 N. Matinise, N. Botha, A. Fall and M. Maaza, Enhanced photocatalytic degradation of methylene blue using zinc vanadate nanomaterials with structural and electrochemical properties, *Sci. Rep.*, 2025, **15**, 26333, DOI: 10.1038/s41598-025-11418-8.

33 G. E. Lau, C. A. C. Abdullah, W. A. N. W. Ahmad, S. Assaw and A. L. T. Zheng, Eco-friendly photocatalysts for degradation of dyes, *Catalysts*, 2020, **10**, 1–16, DOI: 10.3390/catal10101129.

34 H. Huang, L. Liu, Y. Zhang and N. Tian, Novel $BiIO_4$/$BiVO_4$ composite photocatalyst with highly improved visible-light-induced photocatalytic performance for rhodamine B degradation and photocurrent generation, *RSC Adv.*, 2015, **5**, 1161–1167, DOI: 10.1039/c4ra12916d.

35 M. Tanveer, H. H. Cheema, G. Nabi, A. R. Ali, M. K. Hussain and M. A. Qadeer, A novel composite ($BiVO_4$/TiS_2) presenting an excellent Z-scheme photocatalytic degradation for Rhodamine B dye under the visible light irradiation, *J. Lumin.*, 2024, **271**, 120585, DOI: 10.1016/j.jlumin.2024.120585.

36 I. O. Ali, H. Nady, M. I. Mohamed and T. M. Salama, Fabrication and characterization of ZnO and Ag/ZnO nanoparticles for efficient degradation of crystal violet dye in aqueous solution, *J. Indian Chem. Soc.*, 2024, **101**, 101480, DOI: 10.1016/j.jics.2024.101480.

37 M. Farag, S. M. El-Dafrawy and S. M. Hassan, ZnO and C/ZnO Catalysts Synthesized via Plant Mediated Extracts for Photodegradation of Crystal Violet and Methyl Orange Dyes, *J. Inorg. Organomet. Polym. Mater.*, 2024, **34**, 930–943, DOI: 10.1007/s10904-023-02811-9.

38 Y. Luo, W. Zhang, M. Pan, H. Zhang and K. Huang, Hollow Porous Organic Nanosphere-Supported ZnO Composites for Photodegradation of Crystal Violet, *Catalysts*, 2025, **15**, 529, DOI: 10.3390/catal15060529.

39 R. C. Ghaware, N. B. Birajdar, G. S. Kamble and S. S. Kolekar, Degradation of organic Pollutant by Using of $BiVO_4$–$NiFe_2O_4$ Heterostructure Photocatalyst under Visible Light Irradiation: Assessment of Detoxicity Study Using Cirrhinus mrigala, *Langmuir*, 2024, **40**, 14426–14439, DOI: 10.1021/acs.langmuir.4c01136.

40 A. Shafi, N. Ahmad, S. Sultana, S. Sabir and M. Z. Khan, Ag_2S-Sensitized NiO–ZnO Heterostructures with Enhanced Visible Light Photocatalytic Activity and Acetone Sensing Property, *ACS Omega*, 2019, **4**, 12905–12918, DOI: 10.1021/acsomega.9b01261.

41 A. S. Ganie, N. Bashar, S. Bano, S. Hijazi, S. Sultana, S. Sabir and M. Z. Khan, Development and application of redox active GO supported CeO_2/In_2O_3 nanocomposite for photocatalytic degradation of toxic dyes and electrochemical detection of sulfamaxole, *Surf. Interfaces*, 2023, **38**, 102774, DOI: 10.1016/j.surfin.2023.102774.

42 S. I. Wani and A. S. Ganie, Ag_2O incorporated ZnO–TiO_2 nanocomposite: Ionic conductivity and photocatalytic degradation of an organic dye, *Inorg. Chem. Commun.*, 2021, **128**, 108567, DOI: 10.1016/j.inoche.2021.108567.

43 A. S. Ganie, S. Hussain, A. A. Bhat, A. Farooq, R. K. Manavalan, A. M. Fouda, G. Qiao and G. Liu, Preparation of bifunctional Ag_2CO_3 decorated $BiVO_4$ nanospheres for high-performance electrochemical energy storage and photocatalytic activity, *Surf. Interfaces*, 2025, **57**, 105756, DOI: 10.1016/j.surfin.2025.105756.

44 S. Jabeen, A. S. Ganie, N. Ahmad, S. Hijazi, S. Bala, D. Bano and T. Khan, Fabrication and studies of $LaFe_2O_3$/Sb_2O_3 heterojunction for enhanced degradation of Malachite green dye under visible light irradiation, *Inorg. Chem. Commun.*, 2023, **152**, 110729, DOI: 10.1016/j.inoche.2023.110729.

45 P. Luo, Z. Liu, W. Xia, C. Yuan, J. Cheng and Y. Lu, Uniform, Stable, and Efficient Planar-Heterojunction Perovskite Solar Cells by Facile Low-Pressure Chemical Vapor Deposition under Fully Open-Air Conditions, *ACS Appl. Mater. Interfaces*, 2015, **7**, 2708–2714, DOI: 10.1021/am5077588.

46 L. Ni and T. Mo, A new class of high capacity cation-disordered oxides for rechargeable lithium batteries: Li–Ni–Ti–Mo oxides, *Energy Environ. Sci.*, 2015, 12–14, DOI: 10.1039/c5ee02329g.

47 P. D. Sanadi, R. K. Chougale, D. B. Malavekar, J. H. Kim, S. Masimukku, G.-P. Chang-Chien, Y.-C. Ling, S. S. Kolekar and G. S. Kamble, Efficient hydrogen evolution via neutral water electrolysis using nanocrystalline TiO_2 electrocatalyst, *Sci. Rep.*, 2025, **15**, 16074, DOI: 10.1038/s41598-025-93371-0.

48 Q. Ren, J. Liu, Q. Yang and W. Shen, A Review: Photocatalysts Based on BiOCl and g-C_3N_4 for Water Purification, *Catalysts*, 2021, **11**, 1084, DOI: 10.3390/catal11091084.

49 G. S. Kamble, T. S. Natarajan, S. S. Patil, M. Thomas, R. K. Chougale, P. D. Sanadi, U. S. Siddharth and Y.-C. Ling, $BiVO_4$ As a Sustainable and Emerging Photocatalyst: Synthesis Methodologies, Engineering Properties, and Its Volatile Organic Compounds Degradation Efficiency, *Nanomaterials*, 2023, **13**, 1528, DOI: 10.3390/nano13091528.

50 Y.-Y. Lin, P.-H. Lu, F.-Y. Liu, C.-S. Lu and C.-C. Chen, Perovskite-Like Strontium Bismuth Oxyhalides: Synthesis, Characterisation, Photocatalytic Activity and Degradation

© 2026 The Author(s). Published by the Royal Society of Chemistry

Open Access Article. Published on 23 March 2026. Downloaded on 4/30/2026 8:36:08 PM.
This article is licensed under a Creative Commons Attribution-NonCommercial 3.0 Unported Licence.

Mechanism, *Catalysts*, 2023, **13**, 812, DOI: 10.3390/catal13050812.

51 A. Monshi, M. R. Foroughi and M. R. Monshi, Modified Scherrer Equation to Estimate More Accurately Nano-Crystallite Size Using XRD, *World J. Nano Sci. Eng.*, 2012, **2012**, 154–160.

52 T. D. Puttaraju, M. Shashank, H. Raja Naika, G. Nagaraju and M. Manjunatha, Synthesis of bismuth oxychloride nanoparticles via co-precipitation method: Evaluation of photocatalytic activity, *Mater. Today: Proc.*, 2022, **62**, 5533–5539, DOI: 10.1016/j.matpr.2022.04.333.

53 L. Burgio, Bismuth White (Bismuth Oxychloride) and Its Use in Portrait Miniatures Painted by George Engleheart, *Minerals*, 2024, **14**, 723, DOI: 10.3390/min14070723.

54 G. K. Tripathi, K. K. Saini and R. Kurchania, Synthesis of nanoplate bismuth oxychloride—a visible light active material, *Opt. Spectrosc.*, 2015, **119**, 656–663, DOI: 10.1134/s0030400x15100136.

55 H.-L. Chen, W. W. Lee, W.-H. Chung, H.-P. Lin, Y.-J. Chen, Y.-R. Jiang, W.-Y. Lin and C.-C. Chen, Controlled hydrothermal synthesis of bismuth oxybromides and their photocatalytic properties, *J. Taiwan Inst. Chem. Eng.*, 2014, **45**, 1892–1909, DOI: 10.1016/j.jtice.2013.12.015.

56 H. Ma, J. Liu, Y. Wang, S. Zuo, Y. Yu and B. Li, Construction of novel flower-like functionalized black phosphorus nanosheets/P-doped BiOCl S-scheme photocatalysts with improved photocatalytic activity in RhB and Cr(VI) degradation, *Mater. Adv.*, 2022, **3**, 7546–7558, DOI: 10.1039/d2ma00290f.

57 L. Wang, Z. Miao, F. Bi, S. Xiao, L. Zhao, Y. Li, L. Kong, Y. Li, J. Yang, X. Zhang and G. Gai, One-pot room-temperature synthesis of a BiOCl hierarchical microsphere assembled from nanosheets with exposed {001} facets for enhanced photosensitized degradation, *RSC Adv.*, 2022, **12**, 35905–35922, DOI: 10.1039/d2ra06627k.

58 X. Zhang, G. Xu, J. Hu, J. Lv, J. Wang and Y. Wu, Fabrication and photocatalytic performances of BiOCl nanosheets modified with ultrafine Bi_2O_3 nanocrystals, *RSC Adv.*, 2016, **6**, 63241–63249, DOI: 10.1039/c6ra09919j.

59 T. D. Puttaraju, M. Shashank, H. Raja Naika, G. Nagaraju and M. Manjunatha, Synthesis of bismuth oxychloride nanoparticles via co-precipitation method: Evaluation of photocatalytic activity, *Mater. Today: Proc.*, 2022, **62**, 5533–5539, DOI: 10.1016/j.matpr.2022.04.333.

60 N. U. A. Khakwani, M. Aadil, I. Barsoum, Z. Ahmad, G. M. Kamal, M. R. Karim, A. A. Alothman and M. F. Warsi, Tailoring the physical, optical, and structural properties of bismuth oxide to enhance its anionic, cationic, and phenol dye degradation activities, *Ceram. Int.*, 2024, **50**, 33333–33344, DOI: 10.1016/j.ceramint.2024.06.143.

61 P. D. Sanadi, R. K. Chougale, D. B. Malavekar, J. H. Kim, S. Masimukku, G.-P. Chang-Chien, Y.-Y. Lee, R. C. Ghaware, S. S. Kolekar and G. S. Kamble, Controllable synthesis of semiconducting anatase TiO_2 nanostructures for visible light driven photocatalytic degradation of crystal violet and methylene blue dye, *Spectrochim. Acta, Part A*, 2025, **341**, 126404, DOI: 10.1016/j.saa.2025.126404.

© 2026 The Author(s). Published by the Royal Society of Chemistry